F_1 region ion composition in Svalbard during the International Polar Year 2007-2008

Ilkka I. Virtanen[1], Habtamu W. Tesfaw[1], Anita T. Aikio[1], Roger Varney[2], Antti Kero[3], and Neethal Thomas[3]

[1]Space Physics and Astronomy research unit, University of Oulu, Finland
[2]Atmospheric and Oceanic Sciences, University of California Los Angeles, Los Angeles, California, USA
[3]Sodankylä Geophysical Observatory, University of Oulu, Sodankylä, Finland

Key Points:

- We use novel data analysis techniques and chemistry modeling to fit atomic oxygen ion fractions to EISCAT Svalbard radar data during IPY.
- We characterize the F_1 region ion composition dependence on local time, solar zenith angle, and geomagnetic activity.
- The molecular-to-atomic ion transition altitudes are 14–32 km lower than those predicted by the International Reference Ionosphere.

Corresponding author: Ilkka Virtanen, ilkka.i.virtanen@oulu.fi

Abstract

Ions in the F region ionosphere at 150–400 km altitude consist mainly of molecular NO^+ and O_2^+, and atomic O^+. Incoherent scatter (IS) radars are sensitive to the molecular-to-atomic ion density ratio, but its effect to the observed incoherent scatter spectra is almost identical with that of the ion temperature. It is thus very difficult to fit both the ion temperature and the fraction of O^+ ions to the observed spectra. In this paper, we introduce a novel combination of Bayesian filtering, smoothness priors, and chemistry modeling to solve for F_1 region O^+ ion fraction from EISCAT Svalbard IS radar (75.43° corrected geomagnetic latitude) data during the international polar year (IPY) 2007–2008. We find that the fraction of O^+ ions in the F_1 region ionosphere is controlled by ion temperature and electron production. The median value of the molecular-to-atomic ion transition altitude during IPY varies from 187 km at 16–17 MLT to 208 km at 04–05 MLT. The ion temperature has maxima at 05–06 MLT and 15-16 MLT, but the transition altitude does not follow the ion temperature, because photoionization lowers the transition altitude. A daytime transition altitude maximum is observed in winter, when lack of photoionization leads to very low daytime electron densities. Both ion temperature and the molecular-to-atomic ion transition altitude correlate with the Polar Cap North geomagnetic index. The annual medians of the fitted transition altitudes are 14–32 km lower than those predicted by the International Reference Ionosphere.

Plain Language Summary

Ions in the F region ionosphere at 150–400 km altitudes consist mainly of molecular NO^+ and O_2^+, and atomic O^+. Incoherent scatter radars are sensitive to the molecular-to-atomic ion density ratio, but its effect to the observed incoherent scatter spectra is almost identical with that of the ion temperature. It is thus very difficult to fit both the ion temperature and the fraction of O^+ ions to the observed spectra. This causes bias to the fitted temperatures and leaves behaviour of the F_1 region ion composition poorly known. We apply a novel combination of inverse mathematics and chemistry modeling to analysis of EISCAT Svalbard incoherent scatter radar data, and solve for both the ion temperature and the fraction of O^+ ions at the same time. We find that the ion composition is considerably different from a standard model, that it undergoes regular diurnal variations, and it is affected by geomagnetic activity. The typical variations can be qualitatively explained by known diurnal variations in ion temperature, solar photoionization, and ion chemistry. When the ionosphere above Svalbard is in almost complete darkness in mid-winter, ion composition in the daytime ionosphere is considerably different from that observed during the other seasons.

1 Introduction

Typical ion composition in the F region ionosphere makes a smooth transition from molecular NO^+ and O_2^+ below 150 km altitude to almost pure atomic O^+ around 350 km altitude. The ion composition is a key parameter that affects energy exchange rates between the ions and the thermospheric neutral particles, ion and neutral chemistry, and electron recombination speeds. The F region ion composition is a key unknown also in attempts to understand molecular ion upflow and outflow from the ionosphere to the magnetosphere (Takada et al., 2021). However, many aspects of the molecular-to-atomic ion transition remain unknown, because it occurs at too low altitudes for in situ satellite observations, and the ground-based incoherent scatter radar (ISR) observations cannot provide information about the ion composition without limiting assumptions about the ion or electron temperature if conventional analysis tools are used (Evans, 1967; Kelly & Wickwar, 1981). The so-called temperature ion composition ambituity (TICA) (Martínez-Ledesma & Díaz Quezada, 2019) arises from the fact that changes in ion composition and ion temperature can lead to almost identical changes in the incoherent scatter spectra. As a con-

sequence, the ISR data do not only lack the ion composition information, but the ion composition is typically taken from a model, and the ion and electron temperatures fitted to the observed sepctra are biased whenever the true ion composition is different from the model values (Blelly et al., 2010).

Several different approaches have been proposed for solving the TICA problem. Lathuillere et al. (1983) and Lathuillere and Pibaret (1992) used coarse resolutions in time and altitude to reach such a high statistical accuracy in the observed incoherent scatter spectra that both ion temperature and composition could be fitted without any extra information. Kelly and Wickwar (1981) constrained the electron temperature in presence of ion frictional heating and the ion temperature in presence of electron precipitation to enable the ion composition fits. Bjørnå and Kirkwood (1988), Fredriksen (1990), and Aponte et al. (2007) used the incoherent scatter plasma lines to gain the necessary extra information about the electron density and electron temperature to enable the composition fits, and Häggström and Collis (1990) used tri-static electric field measurements and ion energy equation to reach the same goal. The most popular approach to overcome the TICA problem has been the full-profile analysis, in which one assumes that the plasma parameter altitude profiles are smooth, and the ion composition profile is often even assumed to follow some pre-defined shape. These methods include both full-profile solvers that actually fit the plasma parameters to the raw radar data (Cabrit & Kofman, 1997; Litvine et al., 1998), and models to make corrections to the fitted plasma parameters (Shibata et al., 2000; Blelly et al., 2010; Zettergren et al., 2010).

The techniques listed above have not made their way to routine EISCAT radar data analysis for several reasons, for example because coarse altitude resolutions of tens of kilometers and integration times of several minutes are typically not acceptable, the plasma lines are not always detectable and their analysis is tedious, and the true full-profile solvers require considerable computing power if one wants to include also the E region, which requires high altitude resolution, in the same analysis. A computationally light-weight solution that resembles the full-profile analysis, and even extends the principle to an assumption of smoothness in time, was proposed by Virtanen et al. (2021). The Bayesian Filtering Module (BAFIM) is able to fit F_1 region ion compositions in relatively quiet conditions, but the authors concluded that support from a chemistry model would be needed to better capture rapid ion temperature and composition variations in active conditions. Chemistry modeling is already in use in AMISR radar data analysis (Richards et al., 2009), in which the ion composition is modelled in each range gate separately by a chemistry model called the Ion Density Calculator (IDC) (Richards et al., 2010; Richards, 2011). The same chemistry model is used also in the latest versions of the International Reference Ionosphere (Bilitza et al., 2022).

In this paper we combine the BAFIM tool (Virtanen et al., 2021) with the IDC (Richards et al., 2010; Richards, 2011) to carry out IS radar data analysis in a way that produces reliable estimates of the fraction of O^+ ions and ion temperature in the F region. The chemistry model is coupled with BAFIM in such a way that it guides the solver towards physically reasonable solutions, but does not force the final solution to exactly match with the chemistry model. This approach allows us to use the model also when the neutral background ionosphere is not exactly known or when the ions are not in chemical equilibrium. We apply the technique to the almost continuous one-year EISCAT Svalbard incoherent scatter radar run conducted during the International Polar Year (IPY) from March 2007 to February 2008, and study the statistical properties of ion composition, ion temperature, and electron density at 75.43° corrected geomagnetic latitude, corresponding typically to the polar cap location. Statistical results of the F region ion composition from high-latitude radars have been previously provided only by Litvine et al. (1998), who used about 1200 h of data from the EISCAT Tromsø radar site in the auroral oval, and by Shibata et al. (2000) who used 528 h of data from the same site. To our knowledge, our study is the first to provide statistics of F_1 region ion composi-

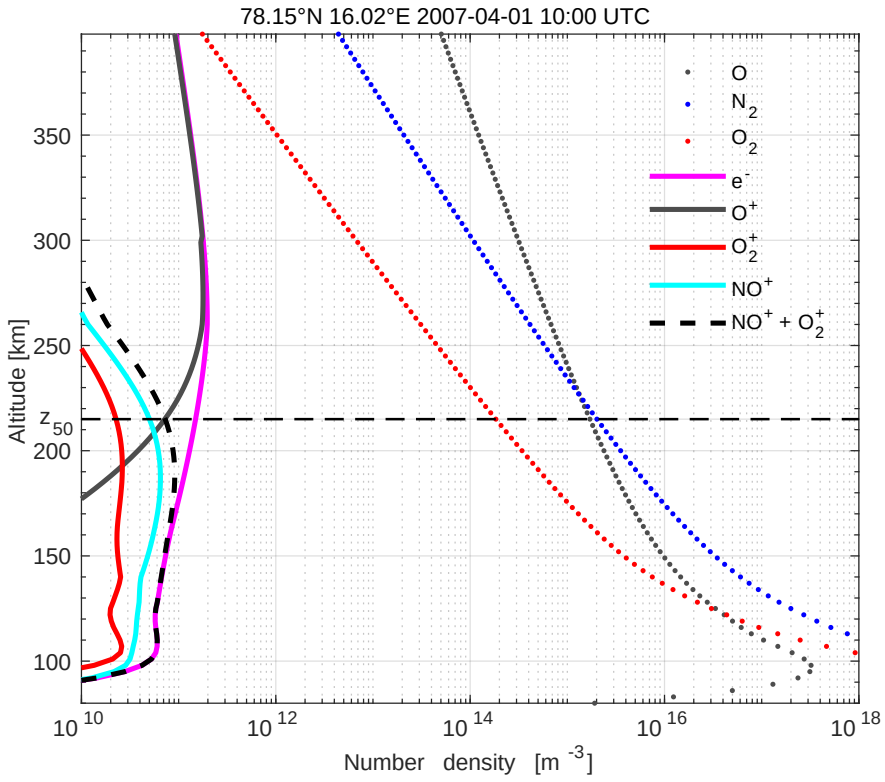

Figure 1. Neutral and charged particle density profiles in Svalbard on April 1 2007 at 10:00 UTC, calculated with the NRLMSISE-00 and IRI-2020 models, respectively. The horizontal dashed line shows the molecular-to-atomic ion transition altitude z_{50}.

tion from a polar cap ISR. Our about 5000 h data set is also larger than those in the previous studies, although it was collected during only one year, during solar minimum conditions.

The paper is organized as follows. In Section 2 we shortly review the typical ion and neutral compositions in the E and F region ionosphere, as well as the basic ion chemical reactions and atmospheric dynamics that alter the ion composition. In Section 3 we introduce the data and the data analysis technique, and give an example of the analysis results. Statistical results from one year of data are presented in Section 4, the key findings are discussed in more detail in Section 5, and the final conclusions are given in Section 6.

2 F-region ion and neutral composition and chemistry

Examples of typical number densities of the major ion and neutral species in the E and F regions of the ionosphere are shown in Figure 1. The ion densities are calculated with the International Reference Ionosphere (IRI) model version 2020 (Bilitza et al., 2022), and the neutral densities with the Naval Research Laboratory Mass Spectrometer and Incoherent Scatter radar (NRLMSISE-00) model (Picone et al., 2002). The model values are calculated for geographic coordinates of the EISCAT Svalbar radar (78.15° N, 16.02 ° E) for 01 April 2007 10:00 UTC. The figure shows that, in this case, the molecular NO^+ and O_2^+ form almost 100 % of the ion density in the E and lower F regions

up to 180 km altitude. A smooth transition from the molecular ions to atomic O^+ takes place between 180 and 270 km altitudes, and the ion gas is almost 100 % O^+ above 270 km. The molecular-to-atomic ion transition altitude z_{50}, where total number density of the molecular ions ($NO^+ + O_2^+$) is equal to the atomic O^+ ion density, is shown as a horizontal dashed line at 215 km altitude. The ion composition reflects altitude variations in the neutral composition, in which the molecular N_2 and the atomic O are the dominant species below and above 230 km altitude, respectively. The altitudes given above are only illustrative, because the densities undergo both diurnal and seasonal variations, and are affected by solar activity.

Ions are produced by solar EUV and soft X ray radiation, impact ionization by precipitating particles, and in chemical reactions. They are lost via recombination and rearrangement reactions. The molecular NO^+ and O_2^+ ions are lost mainly via dissociative recombination in the reactions

$$NO^+ + e \xrightarrow{\alpha_1} N + O, \tag{1}$$
$$O_2^+ + e \xrightarrow{\alpha_2} O + O, \tag{2}$$

where α_1 and α_2 are the reaction rates of the reactions (1) and (2), correspondingly. As recombination of atomic O^+ is very slow, the atomic O^+ ions are lost mainly via rearrangement with neutral N_2 and O_2 in the reactions

$$O^+ + N_2 \xrightarrow{k_1} NO^+ + N, \tag{3}$$
$$O^+ + O_2 \xrightarrow{k_2} O_2^+ + O, \tag{4}$$

where k_1 and k_2 are the corresponding reaction rates. The molecular NO^+ and O_2^+ ions produced in the rearrangement reactions (3) and (4) are subsequently lost via the dissociative recombination reactions (1) and (2). For details of the ion chemical reactions and their reaction rates, we refer to Richards (2011).

The ion composition may undergo rapid variations during ion frictional heating and particle precipitation events. The ion heating speeds up the loss of atomic O^+ and the production of molecular NO^+ in the rearrangement reaction (3) between O^+ and N_2, because the reaction rate k_1 is proportional to square of the ion temperature in high temperatures (Kelly & Wickwar, 1981; Richards, 2011). The heating may also drive thermal expansion of the neutral atmosphere, which increases the neutral N_2 and O_2 densities in the F region and thus speeds up the production of molecular NO^+ and O_2^+ in the rearrangement reactions (3) and (4). On the other hand, the molecular NO^+ and O_2^+ ions undergo dissociative recombination with the free electrons (reactions 1 and 2). The net effect is that ion frictional heating tends to increase the fraction of molecular ions out of the total ion content, but to decrease the total ion (electron) number density. Electron production, either by photoionization or by particle precipitation, increases the total ion density and the fraction of the atomic O^+ ions, because the higher electron density speeds up the dissociative recombination reactions (1) and (2) but does not affect the rearrangement reactions (3) and (4) (Kelly & Wickwar, 1981). The above suggests that the neutral composition, the ion production rate and the ion temperature are the key factors that control the ion composition.

3 Data and data analysis

We use a novel combination of advanced inverse mathematics and chemistry modeling to solve for the electron density N_e, electron temperature T_e, ion temperature T_i, line-of-sight bulk plasma velocity V_i, and the fraction of atomic O^+ ions out of the total ion content p from one year of EISCAT Svalbard radar data, collected during the IPY 2007–2008. This section describes the data and the analysis technique.

3.1 ESR IPY data

From March 2007 until February 2008 the EISCAT Scientific Association operated the EISCAT Svalbard radar (ESR) almost continuously in the same operation mode, as opposed to the usual campaign-based operations with a variety of observation modes. The so-called ipy-mode used the field-aligned 42 m antenna and produced samples of the incoherent scatter autocorrelation function with 6 s time resolution. The experiment covers altitudes from the D region up to 509 km altitude and uses alternating codes (Lehtinen & Häggström, 1987) with 30 μs bit length. The data are sampled with 15 μs sampling steps, which leads to 4.5 km range resolution at "full" (multiples of 30 μs) ACF lags and to 2.25 km resolution at the fractional (15, 45, 75, ... μs) lags (Huuskonen et al., 1996). We call these data "the IPY data".

EISCAT has conducted plasma parameter fits to the IPY data using the Grand Unified Incoherent Scatter Design and Analysis Package (GUISDAP) (Lehtinen & Huuskonen, 1996) and these data are available in the Madrigal data base. The fitted parameters are $N_e, T_e, T_i,$ and V_i. The fraction of O^+ ions p is taken from the IRI model in the standard GUISDAP analysis. It is well known that the IRI ion compositions are inaccurate in the F_1 region, which leads to artefacts in ion and electron temperatures in the standard GUISDAP fits (Blelly et al., 2010; Virtanen et al., 2021).

The IPY data were collected at the very end of solar cycle 23 close to the sunspot minimum. The median Kp index during the IPY year was 1+, hence the period was mostly geomagnetically quiet. The largest value of the Kp index recorded during the whole year was 6-, which was reached in only two three-hour periods in May 24 and August 6, and there were only 21 3-hour intervals with Kp $\geq$ 5. The ESR typically observes the polar cap/cusp ionosphere (Fujiwara et al., 2012), but it may observe also the ionospheric footprint of the closed field lines that connect to the plasma sheet (i.e., the auroral oval), or the different boundary layers in between these regions (Ogawa et al., 2003).

3.2 Ion composition fits and the Bayesian Filtering Module

In ISR plasma parameter fits, one finds such a combination of plasma parameters that a theoretical autocorrelation function of the incoherent scatter signal, as calculated with the selected parameters, matches with the measurements. In the most general form of the incoherent scatter theory, the theoretical autocorrelation function is a function of the number density, temperature, bulk velocity, and ion–neutral collision frequency of each ion species, the corresponding parameters of the electrons, and the magnetic field (Kudeki & Milla, 2011). Simplifying assumptions are needed in practice, because the measurements do not contain sufficient information for estimating all these parameters. The typical assumptions are that all ion species are in the same temperature and drift with the same velocity, and that the ion composition and collision frequencies are equal to model values calculated e.g. with IRI and MSIS. The magnetic field effects are negligible if the radar beam is not very close to perpendicular to the magnetic field. These assumptions lead to the classical four-parameter fit of $N_e, T_e, T_i,$ and V_i. The four-parameter fit is typically used in "gated" F region incoherent scatter analysis, in which one divides the radar beam into discrete intervals called range gates, and fits plasma parameters to the measured autocorrelation function data separately at each gate.

The Bayesian Filtering Module (BAFIM) (Virtanen et al., 2021) is an extension module to the standard EISCAT data analysis tool GUISDAP (Lehtinen & Huuskonen, 1996). BAFIM adds properties of full-profile analysis (Holt et al., 1992; Lehtinen et al., 1996), in which one fits plasma parameters along the whole radar beam at once, to the originally gated analysis tool, and extends the idea of full-profile analysis also to time dimension. When analysing EISCAT radar data with combined BAFIM and GUISDAP, one assumes that the plasma parameter profiles are smooth in both altitude and time. These assumptions are justified when the radar beam is field-aligned and the analysis

proceeds with reasonably short steps in time. The full-profile analysis alone is known to enable ion composition fits (Cabrit & Kofman, 1997; Litvine et al., 1998), and the BAFIM implementation effectively allows one to select resolutions of each plasma parameter separately (Virtanen et al., 2021). One can thus use coarse resolutions for the ion composition and thus improve its accuracy, but still solve the other parameters with better resolutions.

When combined with high range resolution, the original idea of full-profile analysis leads to a large inverse problem, whose solution is computationally heavy. In the BAFIM implementation the actual fit is performed at each altitude separately, and the smoothness assumptions are added by means of Bayesian filtering (Särkkä, 2010, for example) and correlation priors (Roininen et al., 2011). This approach keeps the analysis computationally light-weight. The BAFIM analysis proceeds as a sequence of prediction and update steps. In the prediction step, one produces a prior model of the plasma parameters for the current time step. The prediction is based on the fit results from the previous time step. In the update step, one runs the normal GUISDAP fit of plasma parameters using the prediction as a prior. The smoothness assumptions are built in the prediction step, in which one smooths the plasma parameter profiles in altitude and controls how much the parameters are allowed to change between subsequent time steps. For details of the BAFIM implementation, see Virtanen et al. (2021).

While Virtanen et al. (2021) demonstrated the F_1 region ion composition fits with BAFIM, it was also noted that the tool is not well suited for rapid ion temperature and composition variations. This limits also its use in analysis of large data sets, because such data unavoidably contain also measurements from active conditions. The authors suggested that ion chemistry modeling could be added to the analysis to improve its performance in presence of rapid temperature variations. We note that these issues are related to the F region ion temperature variations and the TICA in particular, and the tool has been successfully used for high-resolution E region analysis in presence of rapid electron density and temperature variations (Tesfaw et al., 2022).

3.3 Ion composition fits with BAFIM and IDC

The Ion Density Calculator (IDC) (Richards et al., 2010; Richards, 2011) is a chemistry model that calculates densities of NO^+, O_2^+, N^+, N_2^+, and O^+ ions. The model assumes that all of the ions except O^+ are in chemical equilibrium, and iteratively finds such an ion composition that the total number density of all ion species matches with a known electron density. In our case the electron density is measured with the radar. The model is based on the chemistry of the Field Line Interhemispheric Plasma (FLIP) ionosphere model (Richards, 2002) and it is included in the latest versions of the IRI (Bilitza et al., 2022).

The IDC model was originally developed for photoionization, but the model works also in presence of auroral particle precipitation, because the additional ion production is implicit in the measured electron density (Richards et al., 2010). Strong ion convection and the produced increase in ion temperature affect the chemical reaction rates and may thus become an issue in modeling (Richards et al., 2010). However, as is explained below, we have coupled the IDC in our analysis tools in such a way that the true temperatures are always used in the model, which guarantees that correct reaction rates are used also when the ions are heated.

We have created an upgraded version of BAFIM that is coupled with the IDC to improve the ion composition fits. We use this tool to fit five plasma parameters, N_e, T_i, $T_r = T_e/T_i$, V_i, and p, to the IPY data. The upgraded BAFIM has two key differences to the original implementation of Virtanen et al. (2021). First, there is an additional upgrade step with the IDC after the GUISDAP fit, and second, the plasma parameters considered as final fit results are those produced by smoothing in altitude.

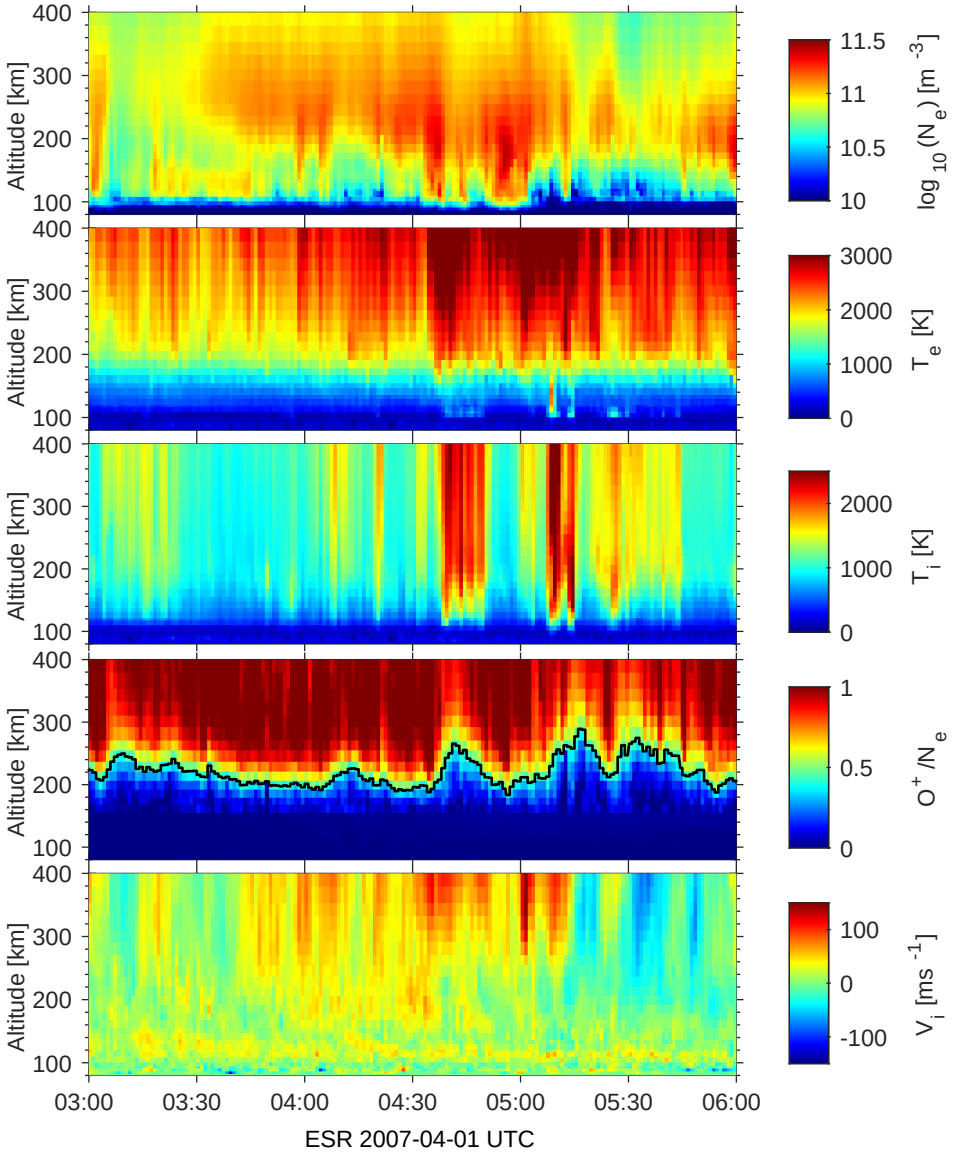

Figure 2. An example of plasma parameter fit results using BAFIM and IDC with GUISDAP from April 2007. From top to bottom, the panels are electron number density, electron temperature, ion temperature, O^+ ion fraction, and line-of-sight plasma velocity (positive away from the radar). The black line in the fourth panel is the molecular-to-atomic transition altitude z_{50}. The solar local time (SLT) is one hour ahead UTC, and the magnetic local time (MLT) is 2.5 hours ahead UTC.

In the IDC step we have plasma parameters $\mathbf{x} = (N_e, T_i, T_r, V_i, p)^T$ and their covariance matrix $\mathbf{P}$ from the GUISDAP fit. We then look for an updated set of parameters $\mathbf{x}' = (N_e', T_i', T_r', V_i', p')^T$ that minimize the cost function

$$S(\mathbf{x}') = (\mathbf{x} - \mathbf{x}')^T \mathbf{P}^{-1} (\mathbf{x} - \mathbf{x}') + \frac{(p' - p_{IDC}(N_e', T_e', T_i'))^2}{\sigma_{IDC}^2}. \quad (5)$$

Here p_{IDC} is the fraction of O^+ ions as calculated with the IDC with N_e', $T_e' = T_r' T_i'$, and T_i' as inputs. The two terms in (5) are penalties for deviations from the GUISDAP fit result and the IDC prediction, respectively. The standard deviation σ_{IDC} is selected by the user and it controls how tightly the updated parameters $\mathbf{x}'$ are bound to the IDC model predictions. With large σ_{IDC} the model has no effect, and with very small σ_{IDC} p' is forced to match with the IDC prediction. We have used $\sigma_{IDC} = 0.1$ in this paper. We emphasize that we do not force the compositions to match with the IDC prediction, but due to the first term in (5) the solution is reasonably close to the GUISDAP fit and the smoothness assumptions of BAFIM are still in place. The final fit results are plasma parameters $\mathbf{x}''$ and their covariance matrix $\mathbf{P}''$ produced by smoothing in altitude by correlation priors, as explained in (Virtanen et al., 2021). The chemistry modeling together with some technical improvements to control of the correlation lengths allow us to use considerably longer time steps than those used by Virtanen et al. (2021) and Tesfaw et al. (2022).

The iterative fit with the cost function (5) also guarantees that the ion and electron temperatures we input to IDC are based on measurements, and that the fitted combination of plasma parameters is reasonable from the chemistry point-of-view. This approach allows us to avoid the issues with temperature dependent reaction rates mentioned by Richards et al. (2010). We might still suffer from biases caused by the neutral atmosphere model (NRLMSISE-00), which naturally does not reproduce thermal expansion of the atmosphre due to short-lived heating events. However, errors in the neutral background tend to produce non-physical bends in the plasma parameter profiles, and this effect is thus minimized by the requirement that the profiles must be smooth in altitude.

We have analysed the whole IPY data with 60 s time resolution using the combination of BAFIM and IDC in GUISDAP. Details of the BAFIM settings used in the analysis and how the input parameters scale with time resolution are give in Appendix A. An example of the fit results is shown in Figure 2, which contains results from 01 April 2007 03–06 UTC . The figure shows five plasma parameters, N_e, T_e, T_i, p, and V_i as function of time and altitude. The electron density profiles (top panel) show several clear electron precipitation events with significant ionization down to the E region. The precipitation also heats the electron gas, producing electron temperature enhancements above 150 km altitude (second panel). The ion temperature profiles (third panel) show a group of strong ion frictional heating events that enhance T_i above 2000 K between 04:30 and 05:30 UTC. Weaker ion heating is seen both before and after the strongest events.

The fourth panel of Figure 2 shows the fraction of O^+ ions p and the molecular-to-atomic transition altitude z_{50} (black line in the fourth panel). The O^+ fraction has the largest fluctuations at 04:30–06:00 UTC, when both electron precipitation and ion frictional heating take place. The frictional heating tends to increase z_{50}, which is rapidly lowered by electron precipitation between the heating events. The bottom panel shows the line-of-sight plasma velocity, including ion upflows in connection to the energy input by electron precipitation and ion frictional heating. A comparison of our fit result and the standard GUISDAP fit from the same time interval is provided as supporting material.

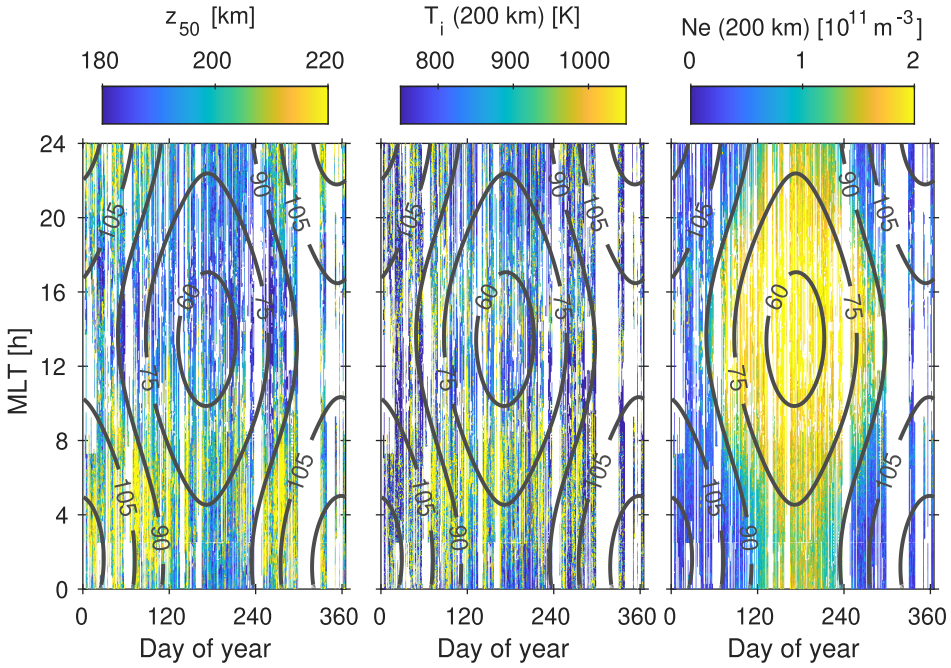

Figure 3. Molecular-to-atomic ion transition altitude (left), ion temperature at 200 km altitude (middle), and electron density at 200 km altitude (right) as function of day of year and magnetic local time . The white areas are missing data due to radar operations in other than the standard IPY mode, or due to technical issues with the radar. Solar zenith angles are shown as contour lines. At 200 km altitude Sun is behind Earth at zenith angles larger than 105°. The solar local time is 1.5 h behind MLT.

4 Statistical results

In this section we present statistical results derived from the IPY data. We concentrate on three key parameters that characterise the F region ion composition variations and their drivers. The parameters are the molecular-to-atomic ion transition altitude z_{50}, ion temperature at 200 km altitude T_i, and electron density at 200 km altitude N_e. The 200 km altitude was selected, because it is close to the average z_{50}. We show also comparisons to model values calculated with the International Reference Ionosphere version 2020, (Bilitza et al., 2022).

4.1 Overview of transition altitudes during the whole year

Figure 3 shows z_{50}, T_i and N_e as function of day of year and magnetic local time (MLT). The MLT has several alternative definitions and it depends on the selected magnetic coordinate system (Laundal & Richmond, 2017). We use the altitude adjusted corrected geomagnetic coordinates (Shepherd, 2014) and calculate the MLT as magnetic longitude difference between the ESR site and a sub-solar point at 700 km altitude. With the ESR coordinates this definition leads to MLT = UTC + 2.5 h on average, which we use for the UTC to MLT conversion. As the IPY started in March, days 1–60 are from year 2008, while the rest are from 2007. The figure shows also contours of the solar zenith angle (SZA) overlaid in each panel.

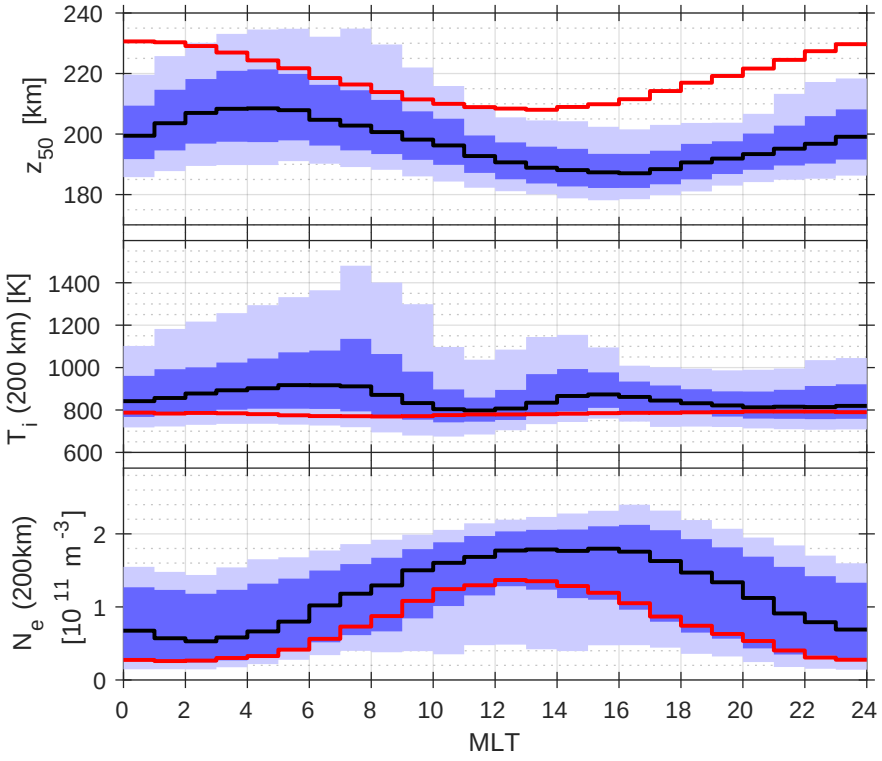

Figure 4. MLT variations of molecular-to-atomic ion transition altitude (top), ion temperature at 200 km altitude (middle) and electron density at 200 km altitude (bottom). The black lines show the median values, the dark blue areas are between 25 % and 75 % percentiles, and the light blue areas are between 10 % and 90 % percentiles. The red lines show medians of IRI-2020 model values.

The transition altitudes in the first panel of Figure 3 show a clear diurnal variation, with largest z_{50} typically observed between magnetic midnight and 10 MLT. The transition altitudes are generally lower during daytime than at night, and the morning maxima are lower during summer than during winter. Ion temperature at 200 km altitude (the second panel of Figure 3) shows also a clear diurnal variation with maxima in the same 00-10 MLT sector with the transition altitude. However, T_i has another local maximum at 14–17 MLT. Main characteristics of N_e (third panel) follow the solar zenith angle contours, indicating that the F_1 region electron density is controlled by photoionization. The daytime and summer maxima in N_e match with the minima in z_{50} (first panel). One should notice that Sun is visible at 200 km altitude when SZA $< 105°$, which means that the F region is always sunlit from March to October and for several hours close to local noon even at mid-winter.

4.2 MLT variations in transition altitude

The MLT variations of z_{50}, T_i and N_e are shown in more detail in Figure 4, which shows median values together with 10 %, 25 %, 75 % and 90 % percentiles in 1-hour MLT bins, as calculated from the whole year of IPY data. The corresponding median values calculated from IRI model predictions are shown as red lines. The transition altitude in the first panel of Figure 4 shows a clear diurnal variation with a maximum median value

208 km at 04-05 MLT and a minimum value 187 km at 16–17 MLT. The IRI prediction shows qualitatively similar night maximum and daytime minimum, but their locations are shifted by about three hours toward earlier MLTs, and the values are up to 32 km larger than our results. Width of the z_{50} distributions, calculated as difference of the 90 % and 10 % percentiles, has a maximum of 45 km at 07–08 MLT and a mimimum of 20 km at 19–20 MLT.

The MLT variations of T_i are shown in the second panel of Figure 4. While T_i shows clear diurnal variations, these variations are substantially different from the z_{50} variations. The ion temperature has two maxima, 920 K at 05–06 MLT and 870 K at 15–16 MLT in the median values. The 75 % and 90 % percentiles have their maxima closer to noon than the median values, at 07–08 MLT in the morning side and 14-15 MLT in the afternoon. The ion temperature is very variable in the morning side, and width of the T_i distribution reaches 760 K at 07–08 MLT. Given that the ion temperature affects the ion composition via the temperature-dependent reaction rates, one might find the large difference between the diurnal variations of median T_i and z_{50} surprising. The IRI prediction does not show significant diurnal variations in T_i.

An explanation to the different behaviours of z_{50} and T_i is given by the electron density, shown in the bottom panel of Figure 4. The electron density is strongly controlled by solar EUV radiation and thus has a dayside maximum after MLT noon and a minimum at 02–03 MLT. In the T_i maximum at 15-16 MLT, the high electron density keeps the fraction of molecular ions and thus also z_{50} low, because the dissociative recombination of NO^+ and O_2^+ is fast when N_e is large. Although the increased ion temperature speeds up the rearrangement of atomic O^+ into molecular NO^+, the molecular ions are lost so rapidly that their fraction of the total ion content cannot become large. In the morning hours the electron density is increasing and the z_{50} maximum at 04–05 MLT is before the T_i maximum at 05–06 MLT, because N_e is lower at 04–05 MLT than an hour later. The IRI prediction of N_e is generally lower than our measurement and maximizes earlier, 12-13 MLT. Underestimation of F_1 region N_e by previous versions of IRI in Svalbard has been reported by (Bjoland et al., 2016). One can also see that the IRI z_{50} is controlled by the IRI N_e variations, which may be expected as the IRI T_i is almost constant.

4.3 Solar zenith angle dependence of the transition altitude

While one may reasonably assume that the MLT variations in ion temperature are mainly due to the varying location of the radar with respect to the plasma convection cells, the variations in electron density are largely due to variations in solar illumination. It is thus illustrative to study the variations also as function of solar zenith angle, as shown in Figure 5. The data points from before and after local noon are shown separately, because there is a clear asymmetry between the morning and evening sides.

The electron densities in the third panel of figure 5 show a clear SZA dependence as expected, and the narrow distributions indicate that the density is primarily controlled by the solar radiation. In the morning side, the densities are almost constant for 125°–100° zenith angles, and they increase monotonically with decreasing zenith angle for zenith angles 100°–55°. In the evening side the electron densities are generally larger than in the morning side, and the densities still decrease also at zenith angles larger than 100°. This might be due to the long lifetime of the O^+ ions and plasma transport from the dayside. The zenith angle dependence of N_e continues to angles larger than 90°, because the solar radiation can still reach the atmosphere due to curvature of the Earth. With 100° zenith angle the incoming radiation has passed through the ionosphere at 100 km altitude, which is enough for majority of the ionizing radiation to be absorbed.

The ion temperatures in the second panel of figure 5 do not show strong SZA dependence, but they are more variable in the morning side than in the evening side, and

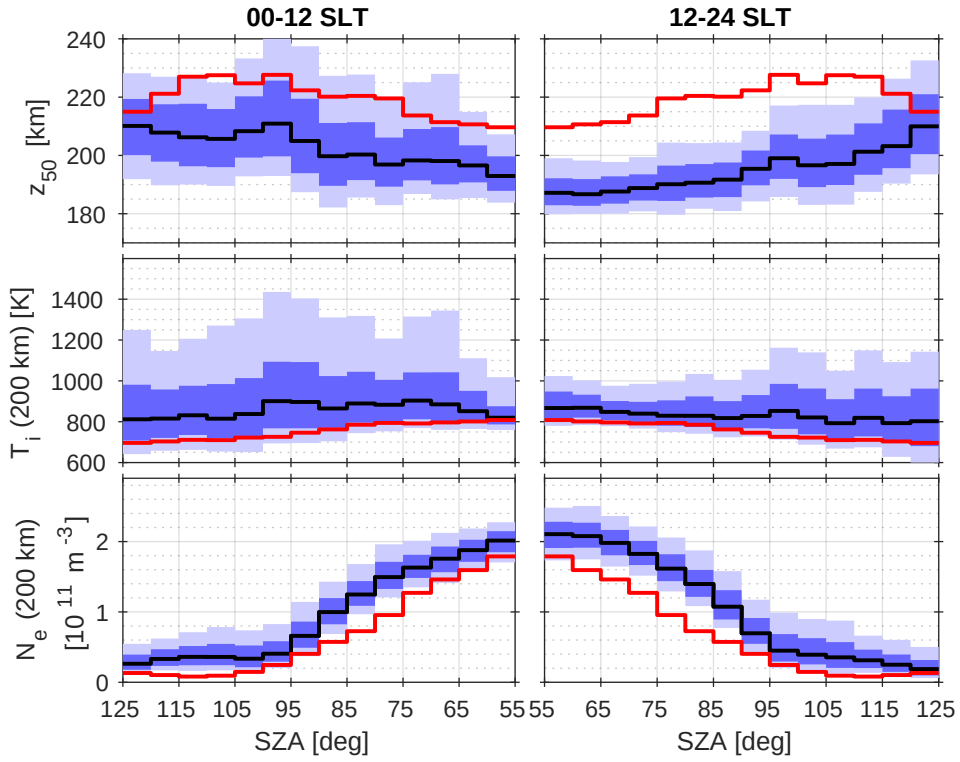

Figure 5. Solar zenith angle variations in the same format as in Figure 4, for morning and evening sides separately.

have interesting small maxima at the 90–100° zenith angles. The transition altitude z_{50} in the first panel of figure 5 shows clear variations with SZA, with smallest and largest values at smallest and largest zenith angles, correspondingly. The z_{50} variations match well with those of the electron density, large electron densities corresponding to low z_{50}, superimposed with some effects from the relatively stable ion temperature. Like T_i, also z_{50} shows interesting local maxima close to sunset at 95-100° zenith angles. The mechanism that causes the local z_{50} maxima remains unclear, but could be related to atmospheric dynamics or transient ion chemistry effects at the Solar terminator.

4.4 Seasonal variations

Figure 6 shows median values of z_{50}, T_i and N_e as function of MLT, but separately for winter, equinoxes, and summer. The seasons are centred on solstices and equinoxes, and each data point belongs to the season whose centre is closest to it. The spring and autumn data are merged to form one equinox data set because they behave similarly. With this division the whole winter has SZA $\geq 95°$ and the whole summer has SZA $\leq 85°$, but the equinox data set has twice as much data points as the winter and summer ones. We note that we have only one year of IPY data and the results thus reflect the variations typical for a deep solar minimum year.

The figure shows that the morning side maxima of z_{50} and T_i are both at 07–08 MLT on summer. The maxima are at the same time, because the electron density increases very smoothly with MLT during summer mornings. The overall high N_e in summer also

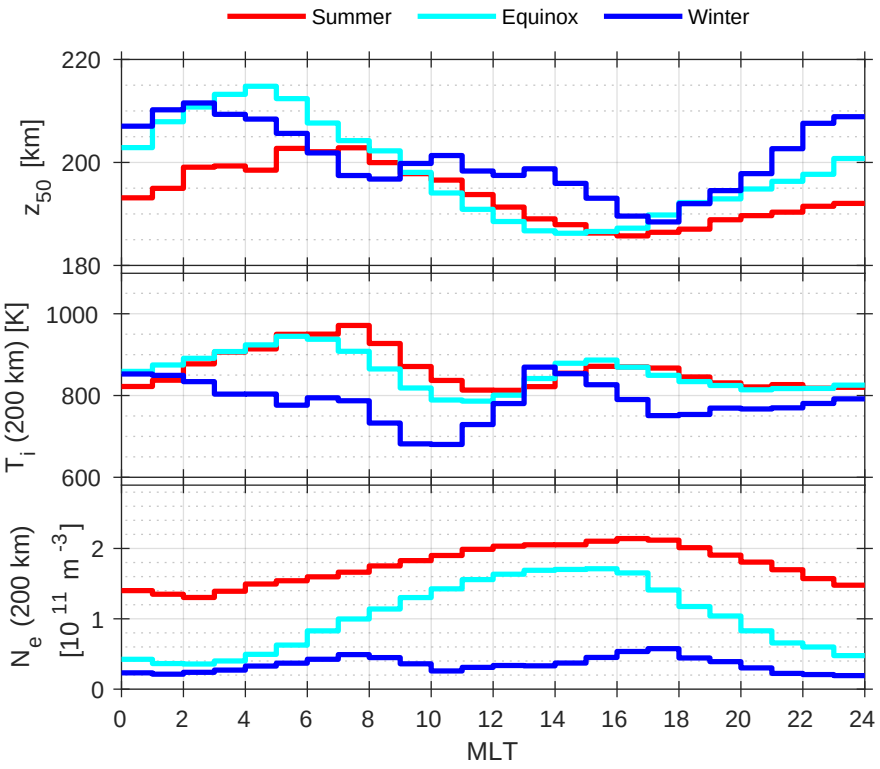

Figure 6. MLT variations of molecular-to-atomic ion transition altitude (top), ion temperature at 200 km altitude (middle), and electron density at 200 km altitude, separetely for summer (red), equinoxes (cyan), and winter (blue).

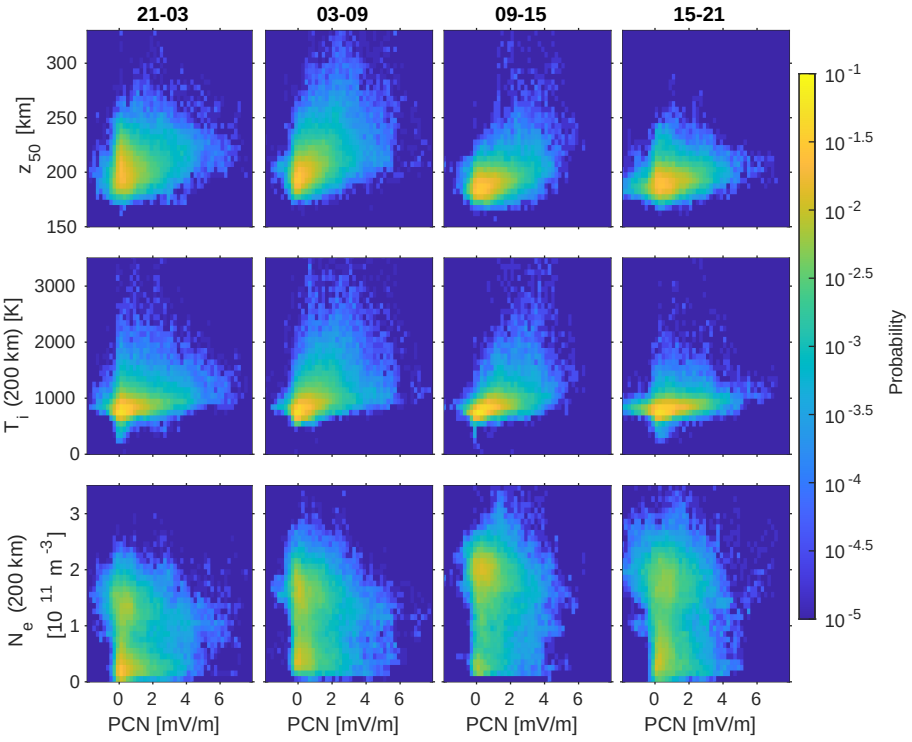

Figure 7. Distribution of fit results as function of the PCN index and the molecular to atomic transition altitudes (top row), the PCN index and ion temperature at 200 km altitude (middle row), and the PCN index and electron density at 200 km altitude (bottom row). Each column of panels corresponds to a SLT bin shown on the top. Notice the logarithmic color scale.

favors the atomic ions, and the maximum z_{50} in summer is only 203 km. The evening side T_i maximum at 16–17 MLT does not create a maximum in transition altitude because the electron densities are high at this time. During equinoxes, the morning side T_i maximum moves to 05–06 MLT and the z_{50} maximum of 215 km occurs one hour earlier, 04–05 MLT. The MLT difference is probably due to a large gradient in N_e, which favours large fractions of molecular ions at earlier MLTs when the electron density is lower. The evening side maximum in T_i coincides with large N_e also during equinoxes, which keeps z_{50} low despite the ion heating.

The winter data in Figure 6 are quite different from summer and equinoxes. The transition altitude has a morning side maximum at 02–03 MLT, separated by two hours from the T_i maximum at 00-01 MLT, but still in a region with relatively high T_i. A distinct feature of the winter data is a daytime maximum in z_{50} and a corresponding minimum in N_e. The winter time electron densities are very low in general, and the density has two maxima at 07–08 and 17–18, because photoionization is practically non-existent and the F region density is created mainly by soft precipitation. The daytime maximum in z_{50} is caused by the N_e minimum. This phenomenon will be discussed in more detail in Section 5.1.

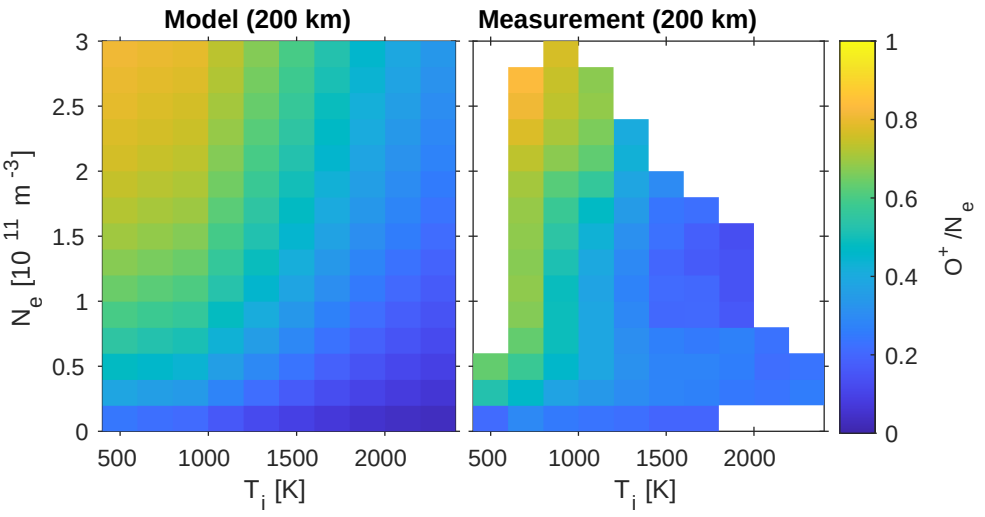

Figure 8. Left: Model results of O^+ ion fraction at 200 km altitude as function of T_i and N_e. The composition is calculated with the IDC model using neutral background atmosphere from NRLMSISE-00 for Svalbard on March 21, 2007 at 05 UTC. Right: Measured O^+ ion fraction at 200 km altitude as function of T_i and N_e. The medians are calculated from one year of ESR data. Only bins that contain at least 100 data points are shown.

4.5 Correlation with geomagnetic activity

As ion temperature is a key parameter that affects the ion composition, one may reasonably assume that the ion composition should correlate with the level of geomagnetic activity via increased ion frictional heating. Figure 7 shows distributions of fitted transition altitudes (top), ion temperatures at 200 km altitude (middle), and electron densities at 200 km altitude (bottom) as function of the Polar Cap North (PCN) index (Troshichev et al., 2006). The index is a measure of the solar wind merging electric field and it estimates the polar cap magnetic activity generated by the solar wind magnetosphere interaction. The data are divided into four equally sized blocks according to the solar local time (SLT = MLT − 1.5 h).

The results show that both z_{50} and T_i increase with increasing PCN when PCN is positive. The strongest response occurs 03–09 SLT and the effect weakens towards the evening, the weakest response being observed 15-21 SLT. The strongest response to PCN in both z_{50} and T_i is located in the same local time sector with the generally highest ion temperatures (Figure 4). This is expected, because the T_i maximum suggests that plasma convection leads to strongest ion frictional heating in this sector. The response is weaker in the 09-15 SLT bin, where the electron density is high, and in the 15-21 SLT bin, where the electron density is higher than in the morning side and the ion temperatures are lower in general. The electron densities do not show clear PCN dependence.

5 Discussion

5.1 Effects of N_e and T_i in the F_1 region ion composition

Variations in the molecular-to-atomic ion transition altitude were connected to variations in electron density and ion temperature in Section 4. It is thus illustrative to study in more detail how the F_1 region ion composition responds to changes in N_e and T_i. The

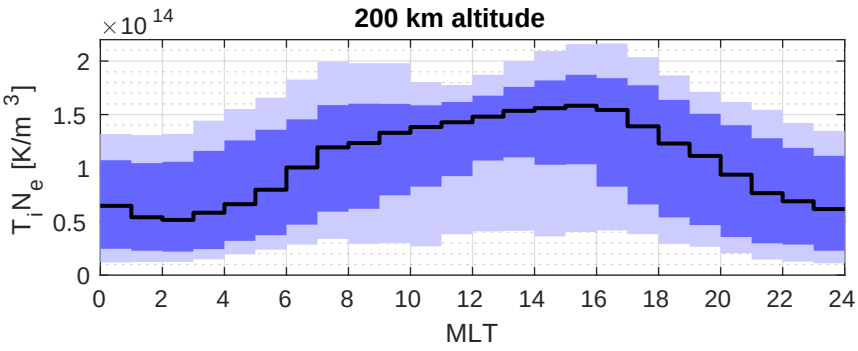

Figure 9. MLT variations of the product T_iN_e (at 200 km). The black line is the median over the whole year, and the shaded areas show the 10 %, 25 %, 75 %, and 90 % percentiles.

left panel of Figure 8 shows a model calculation of the fraction of O^+ ions as function of ion temperature and electron density. Electron and ion temperatures are assumed to be equal, and the neutral background atmosphere is taken from the NRLMSISE-00 model for March 21 2007 a 05:00 UTC at 200 km altitude. The results demonstrate how high electron densities and low ion temperatures favor atomic O^+ ions, while low densities and high ion temperatures favor the molecular ions, as discussed in the earlier sections. Regarding the winter daytime maximum in z_{50}, the figure shows that the fraction of O^+ ions is always low when the electron density is of the order of $10^{10}\mathrm{m}^{-3}$.

Distribution of the fitted O^+ fractions at 200 km altitude during the whole IPY year are shown on the right in Figure 8. The figure is in good qualitative agreement with the model calculations on the left, which correspond to only one particular instant of time and neutral background atmosphere. The measurements do not cover all combinations of T_i and N_e, because solar radiation will necessarily heat the ionosphere so that combinations of high N_e and extremely low T_i are impossible, while high T_i speeds up the recombination and thus prevents the combinations of high T_i and high N_e.

5.2 Diurnal variations of transition altitude and ion temperature

The Joule heating pattern in the auroral oval is known to have maxima in the dawn side and in the dusk side, due to convection electric fields (Cai et al., 2016, and references therein). However, the ESR is typically in the polar cap, and Cai et al. (2016) found only the afternoon Joule heating maximum around 15 MLT from ESR measurements. The Joule heating pattern observed by Cai et al. (2016) thus cannot directly explain our observations of z_{50}, which peaks in the morning side, and T_i, which has two maxima.

A key difference between our results and the Joule heating studies is that the ion temperature is proportional to kinetic energy per particle, while the Joule heating rates are expressed as power per unit volume. The same Joule heating rate may thus lead to different ion temperatures, depending on the ion (electron) density. In our data the morning side ion temperature maximum at 05–07 MLT (Figure 4) is actually larger than the afternoon maximum at 15–16 MLT, but N_e is considerably lower around the morning side maximum. The morning side T_i maximum may thus be generated with considerably smaller heating power per unit volume than the afternoon maximum. This is demonstrated in Figure 9, which shows the product T_iN_e as function of MLT. The product is proportional to the kinetic energy per unit volume and can thus be compared with Joule heating rates. The median values of T_iN_e do not have a morning side maximum, because the T_i maximum is smoothed out by the lower N_e. The product has maximum at 15–

16 MLT, which is exactly the MLT bin where Cai et al. (2016) found the afternoon hot spot in Joule heating.

The afternoon hot spot in Joule heating does not create a z_{50} maximum in summer and equinoxes (see Figure 6), because ion production by photoionization keeps the electron density high, which favours the atomic ions. An exception is winter, when there is no photoionization and z_{50} is clearly elevated close to the afternoon maximum in T_i, as one can see from Figure 6. However, the day-side maximum in z_{50} does not coincide with the afternoon maximum in T_i even at winter, because the very low electron density between 10 and 11 MLT creates the z_{50} maximum there.

The morning side maximum in Joule heating creates both T_i and z_{50} maxima in all seasons, as illustrated in Figure 6. This is because the electron densities are generally lower before 8 MLT than 13–16 MLT. The effect of electron density is still visible also in the morning side maximum, where the transition altitudes are clearly lower in summer than during other seasons, because the electron densities in the 00-08 MLT sector are much higher in summer than at other times of the year.

5.3 Limitations of the analysis method and potential future work

The BAFIM analysis assumes that the plasma parameters vary smoothly in both time and range (altitude). Incorrect use of such assumptions could obviously lead to incorrect analysis results if sharp gradients were present in the ionosphere. In BAFIM the smoothness is expressed in terms of probabilities, and also relatively sharp gradients may be produced if the measurements give strong enough evidence about their existence. For example, relatively sharp temporal gradients are seen in all plasma parameters in Figure 2. The assumption of smoothness in range is well justified in field-aligned observations, because the high ion and electron mobilities along the field-line prevent generation of large gradients. The gradients tend to be larger in the E and lower F regions than above, which we take into account by means of using shorter correlation lengths in these regions (Virtanen et al., 2021). We thus believe that the smoothness assumptions do not significantly bias the results from field-aligned observations, but the method may not be applicable to other beam directions in its present form. However, prior models very similar to those used in BAFIM are used for 4-dimensional (three spatial dimensions plus time) ionospheric tomography (Norberg et al., 2023). These techniques could possibly be generalized to volumetric plasma parameter fits with the multi-beam EISCAT3D radar (McCrea et al., 2015).

The IDC assumes chemical equilibrium of all other ion species except O^+, and takes the neutral background atmosphere from the empirical NRLMSISE-00 model. These assumptions may affect the chemistry modeling in active conditions, in which the chemistry may not have time to reach equilibrium, and energy input from the magnetosphere may lead to thermal expansion of the neutral atmosphere. The way we have coupled BAFIM and IDC reduces these effects to the smallest possible level, because IDC is used merely to guide the solver toward a physically reasonable solution, and the smoothness assumptions in BAFIM efficiently suppress artifacts created by inaccurate chemistry modeling. For example, the chemistry modeling could overestimate the fraction of molecular ions in very short-lived frictional heating events, during which the ionosphere is not in chemical equilibrium. However, the overestimation would lead to unrealistic local ion temperature maxima, which would be suppressed by the smoothness assumptions.

We implicitly assume that the true average ion temperature can be estimated from the field-aligned radar data using a standard incoherent scatter theory that assumes Maxwellian particle velocity distributions. This assumption may not be valid during very strong heating events, which generate T_i anisotropies with higher T_i in the directions perpendicular to the magnetic field than along the field, and toroidal ion velocity distributions in the F region (Goodwin et al., 2014, and references therein). The average ion tempera-

ture that is relevant for the chemistry might thus be larger than the field-aligned temperature extracted from the radar data, and even the field-aligned temperature could be biased in the worst case. Ion temperature anisotropies could thus lead to underestimation of molecular ion content during intense heating events. As the T_i anisotropy takes place throughout the F region, it might not create noticeable artifacts in the plasma parameter profiles. While the T_i anisotropies might have a significant effect during some very strong heating events, vast majority of our data are measured in relatively quiet geomagnetic conditions and are free from the temperature anisotropy effects. However, this effect is worth considering if one studies strong, individual heating events.

6 Conclusions

In this paper, we have developed a new analysis tool for IS radar data by coupling the BAFIM tool (Virtanen et al., 2021) with the IDC ion chemistry model (Richards et al., 2010; Richards, 2011). By using the tool, we have fitted the F_1 region O^+ ion fractions (O^+/N_e) to one year of EISCAT Svalbard radar IPY data from March 2007 to February 2008 close to solar minimum.

When averaged over the whole year, the molecular-to-atomic ion transition altitude z_{50} undergoes diurnal variations with a maximum median value of 208 km at 04–05 MLT and a minimum of 187 km at 16–17 MLT. The diurnal variation in z_{50} is a combined effect of variations in T_i and N_e. Increasing T_i tends to increase z_{50}, while increasing N_e tends to decrease it. T_i has two maxima, 920 K at 05–06 MLT and 870 K at 15–16 MLT, but the global maximum in z_{50} is already 04–05 MLT when N_e is smaller than closer to the noon. The T_i maximum at 15–16 MLT does not increase z_{50}, because the high N_e during these MLTs favors the atomic O^+ ions.

We find that the electron density follows variations in the solar zenith angle, indicating that photoionization is the dominant electron production mechanism. An exception is the winter, when photoionization is very weak and N_e has a daytime minimum surrounded by weak maxima at 07–08 MLT and 17–18 MLT. These maxima are probably caused by soft precipitation. The very low daytime N_e leads to anomalously large fraction of molecular ions in the winter daytime F_1 region.

The ion temperature and the molecular-to-atomic transition altitude show correlation with the Polar Cap North (PCN) geomagnetic index. The strongest correlations are observed 03–09 SLT, which is close to the morning side maximum in T_i. The weakest response is seen 15–21 SLT, when N_e is high and T_i relatively low, in average. The electron density does not show significant response to PCN.

Our observed z_{50} is clearly different from that predicted by the International Reference Ionosphere. The IRI predictions show MLT variations qualitatively similar with our results, but the annual median values are 14–32 km larger in IRI than in our observations, and the maximum and minimum values are at 3 hours earlier MLTs. These differences are related to the generally lower T_i and N_e in IRI than in our measurements, and to lack of diurnal T_i variations in IRI.

7 Open Research

A download link to BAFIM will be provided upon acceptance of the manuscript. We use the Flipchem python interface to the IDC package (Reimer et al., 2021), available from `https://doi.org/10.5281/zenodo.3688853`. The EISCAT data are available for download from the EISCAT data server: `https://portal.eiscat.se/schedule/`.

Table A1. BAFIM settings used in the data analysis. N_e, T_i, T_r, and V_i are fitted at all altitudes above h_{min}. The constants s^h and s^t are scaling factors that control smoothness of the solutions in range and time, respectively, as explained in the text.

	s^h ($s^{-1/2}$)	s^t	h_{min} (km)	h_{max} (km)
N_e	0.05	$2.5 \cdot 10^{11}$ $\mathrm{m^{-3}s^{-1/2}}$	0	-
T_i	0.1	30 $\mathrm{Ks^{-1/2}}$	80	-
T_r	0.1	0.03 $\mathrm{s^{-1/2}}$	97	-
V_i	0.05	2.5 $\mathrm{ms^{-3/2}}$	80	-
p	0.05	0.01 $\mathrm{s^{-1/2}}$	150	500

Appendix A BAFIM settings

For this work the BAFIM implementation of Virtanen et al. (2021) was slightly modified to make the tool better suited for the large-scale data analysis and to couple it with the IDC model. For description of the coupling with the IDC we refer to Section 3.3, and for the general BAFIM implementation we refer to Virtanen et al. (2021). In this section we describe the length scales and time scales used to control smoothness in altitude and time, and how these were changed from Virtanen et al. (2021).

As explained in Section 3 of Virtanen et al. (2021), the smoothness in altitude is controlled by means of the lengths scales s_i^h, where the index i refers to each fitted plasma parameter, and the smoothness in time is controlled by a similar scaling factors s_i^t. The final correlation lengths in altitude are products $s_i^h H$, where H is the local plasma scale height, and the final process noise variance in the Bayesian filtering is the product $\left(s_i^t\right)^2 \Delta t$, where Δt is the time step duration. The correlation priors (Roininen et al., 2011) make the smoothing in altitude independent from the altitude resolution, and the process noise variances scale with the time step duration to adjust for different time resolutions.

One remaining effect that was not considered by Virtanen et al. (2021) is that the correlations in time introduced by the Bayesian filtering propagate information about smoothness in altitude in between adjacent time steps. The smoothing in altitude was thus stronger than one could expect based on the correlation lengths alone. The effect becomes clearly visible when one moves from the approximately 5 s time resolution of (Virtanen et al., 2021) to the 60 s resolution used in this paper. To accommodate for this effect, we multiply the length scales s_i^h by square root of the time step duration Δt. The length scales are thus given in units $\mathrm{s^{-1/2}}$ and the final correlation length is the product $s_i^h \Delta t^{-1/2} H$. The parameters used in the BAFIM analysis presented in this paper are listed in Table A1.

Acknowledgments

We acknowledge the EISCAT Scientific Association for the radar data. EISCAT is an international association supported by research organisations in China (CRIRP), Finland (SA), Japan (NIPR and ISEE), Norway (NFR), Sweden (VR), and the United Kingdom (UKRI). The authors wish to acknowledge CSC – IT Center for Science, Finland, for computational resources. This work was supported by the Kvantum Institute of the University of Oulu, by the Academy of Finland (347796 and 24304299), and by the Vilho, Yrjö and Kalle Väisälä foundation of the Finnish Academy of Science and Letters.

References

Aponte, N., Sulzer, M. P., Nicolls, M. J., Nikoukar, R., & González, S. A. (2007).

Molecular ion composition measurements in the F1 region at Arecibo. *Journal of Geophysical Research: Space Physics*, *112*(6), 1–18. doi: 10.1029/2006JA012028

Bilitza, D., Pezzopane, M., Truhlik, V., Altadill, D., Reinisch, B. W., & Pignalberi, A. (2022). The International Reference Ionosphere model: A review and description of an ionospheric benchmark. *Reviews of Geophysics*. doi: 10.1029/2022RG000792

Bjoland, L. M., Belyey, V., Løvhaug, U. P., & La Hoz, C. (2016, 9). An evaluation of International Reference Ionosphere electron density in the polar cap and cusp using EISCAT Svalbard radar measurements. *Annales Geophysicae*, *34*(9), 751–758. doi: 10.5194/angeo-34-751-2016

Bjørnå, N., & Kirkwood, S. (1988). Derivation of ion composition from a combined ion line/plasma line incoherent scatter experiment. *Journal of Geophysical Research*, *93*(A6), 5787. doi: 10.1029/JA093iA06p05787

Blelly, P. L., Alcaydé, D., & Van Eyken, A. P. (2010). A new analysis method for determining polar ionosphere and upper atmosphere characteristics from ESR data: Illustration with IPY period. *Journal of Geophysical Research: Space Physics*, *115*(9), 1–12. doi: 10.1029/2009JA014876

Cabrit, B., & Kofman, W. (1997). Ionospheric composition measurement by EISCAT using a global fit procedure. *Annales Geophysicae*, *14*(12), 1496–1505. doi: 10.1007/s00585-996-1496-2

Cai, L., Aikio, A. T., & Milan, S. E. (2016). Joule heating hot spot at high latitudes in the afternoon sector. *Journal of Geophysical Research: Space Physics*, *121*(7), 7135–7152. doi: 10.1002/2016JA022432

Evans, J. V. (1967, 7). Electron temperature and ion composition in the F1 region. *Journal of Geophysical Research*, *72*(13), 3343–3355. doi: 10.1029/jz072i013p03343

Fredriksen, (1990). High latitude quiet summer ion composition profiles derived from a combined ion line/plasma line incoherent scatter experiment. *Journal of Atmospheric and Terrestrial Physics*, *52*(1), 77–84. doi: 10.1016/0021-9169(90)90117-6

Fujiwara, H., Nozawa, S., Maeda, S., Ogawa, Y., Miyoshi, Y., Jin, H., ... Terada, K. (2012). Polar cap ionosphere and thermosphere during the solar minimum period: EISCAT Svalbard radar observations and GCM simulations. *Earth, Planets and Space*, *64*(6), 459–465. doi: 10.5047/eps.2011.05.023

Goodwin, L., St.-Maurice, J. P., Richards, P., Nicolls, M., & Hairston, M. (2014). F region dusk ion temperature spikes at the equatorward edge of the high-latitude convection pattern. *Geophysical Research Letters*, *41*(2), 300–307. doi: 10.1002/2013GL058442

Häggström, I., & Collis, P. (1990). Ion composition changes during F-region density depletions in the presence of electric fields at auroral latitudes. *Journal of Atmospheric and Terrestrial Physics*, *52*(6-8), 519–529. doi: 10.1016/0021-9169(90)90050-W

Holt, J. M., Rhoda, D. A., Tetenbaum, D., & van Eyken, A. P. (1992). Optimal analysis of incoherent scatter radar data. *Radio Science*, *27*(3), 435–447. doi: 10.1029/91RS02922

Huuskonen, A., Lehtinen, M. S., & Pirttilä, J. (1996). Fractional lags in alternating codes: Improving incoherent scatter measurements by using lag estimates at noninteger multiples of baud length. *Radio Science*, *31*(2), 245–261. doi: 10.1029/95RS03157

Kelly, J. D., & Wickwar, V. B. (1981). Radar measurements of high-latitude ion composition between 140 and 300 km altitude. *Journal of Geophysical Research: Space Physics*, *86*(A9), 7617–7626. doi: 10.1029/JA086iA09p07617

Kudeki, E., & Milla, M. A. (2011). Incoherent scatter spectral theories - Part I: A general framework and results for small magnetic aspect angles. *IEEE Trans-*

actions on Geoscience and Remote Sensing, *49*(1 PART 2), 315–328. doi: 10.1109/TGRS.2010.2057252

Lathuillere, C., Lejeune, G., & Kofman, W. (1983). Direct measurements of ion composition with EISCAT in the high-latitude F1 region. *Radio Science*, *18*(6), 887–893. doi: 10.1029/RS018i006p00887

Lathuillere, C., & Pibaret, B. (1992). *A statistical model of ion composition in the auroral lower F region* (Vol. 12; Tech. Rep. No. 6). doi: 10.1016/0273-1177(92)90048-3

Laundal, K. M., & Richmond, A. D. (2017, 3). Magnetic Coordinate Systems. *Space Science Reviews*, *206*(1-4), 27–59. doi: 10.1007/s11214-016-0275-y

Lehtinen, M. S., & Häggström, I. (1987). A new modulation principle for incoherent scatter measurements. *Radio Science*, *22*(4), 625–634. doi: 10.1029/RS022i004p00625

Lehtinen, M. S., & Huuskonen, A. (1996). General incoherent scatter analysis and GUISDAP. *Journal of Atmospheric and Terrestrial Physics*, *58*(1-4), 435–452. doi: 10.1016/0021-9169(95)00047-X

Lehtinen, M. S., Huuskonen, A., & Pirttilä, J. (1996). First experiences of full-profile analysis with GUISDAP. *Annales Geophysicae*, *14*(12), 1487–1495. doi: 10.1007/s00585-996-1487-3

Litvine, A., Kofman, W., & Cabrit, B. (1998). Ion composition measurements and modelling at altitudes from 140 to 350 km using EISCAT measurements. *Annales Geophysicae*, *16*(10), 1159. doi: 10.1007/s005850050685

Martínez-Ledesma, M., & Díaz Quezada, M. A. (2019). Determination of the Signal Fluctuation Threshold of the Temperature-Ion Composition Ambiguity Problem Using Monte Carlo Simulations. *Journal of Geophysical Research: Space Physics*, *124*(4), 2897–2919. doi: 10.1029/2018JA026217

McCrea, I., Aikio, A., Alfonsi, L., Belova, E., Buchert, S., Clilverd, M., ... Vierinen, J. (2015, 12). The science case for the EISCAT_3D radar. *Progress in Earth and Planetary Science*, *2*(1), 21. doi: 10.1186/s40645-015-0051-8

Norberg, J., Käki, S., Roininen, L., Mielich, J., & Virtanen, I. I. (2023, 1). Model-Free Approach for Regional Ionospheric Multi-Instrument Imaging. *Journal of Geophysical Research: Space Physics*, *128*(1). doi: 10.1029/2022JA030794

Ogawa, Y., Fujii, R., Buchert, S. C., Nozawa, S., & Ohtani, S. (2003). Simultaneous EISCAT Svalbard radar and DMSP observations of ion upflow in the dayside polar ionosphere. *Journal of Geophysical Research: Space Physics*, *108*(A3). doi: 10.1029/2002JA009590

Picone, J. M., Hedin, A. E., Drob, D. P., & Aikin, A. C. (2002). NRLMSISE-00 empirical model of the atmosphere: Statistical comparisons and scientific issues. *Journal of Geophysical Research: Space Physics*, *107*(A12), 1–16. doi: 10.1029/2002JA009430

Reimer, A., amisr user, & FGuenzkofer. (2021, November). *amisr/flipchem: v2021.2.2 bugfix release*. Zenodo. doi: 10.5281/zenodo.5719844

Richards, P. G. (2002). Ion and neutral density variations during ionospheric storms in September 1974: Comparison of measurement and models. *Journal of Geophysical Research: Space Physics*, *107*(A11). doi: 10.1029/2002JA009278

Richards, P. G. (2011). Reexamination of ionospheric photochemistry. *Journal of Geophysical Research: Space Physics*, *116*(8), 1–15. doi: 10.1029/2011JA016613

Richards, P. G., Bilitza, D., & Voglozin, D. (2010). Ion density calculator (IDC): A new efficient model of ionospheric ion densities. *Radio Science*, *45*(5), 1–11. doi: 10.1029/2009RS004332

Richards, P. G., Nicolls, M. J., Heinselman, C. J., Sojka, J. J., Holt, J. M., & Meier, R. R. (2009). Measured and modeled ionospheric densities, temperatures, and winds during the international polar year. *Journal of Geophysical Research: Space Physics*, *114*(12). doi: 10.1029/2009JA014625

751 Roininen, L., Lehtinen, M. S., Lasanen, S., Orispää, M., & Markkanen, M. (2011).
752 Correlation priors. *Inverse Problems and Imaging*, *5*(1), 167–184. doi: 10
753 .3934/ipi.2011.5.167
754 Särkkä, S. (2010). Bayesian filtering and smoothing. *Bayesian Filtering and Smooth-*
755 *ing*, 1–232. doi: 10.1017/CBO9781139344203
756 Shepherd, S. G. (2014, 9). Altitude-adjusted corrected geomagnetic coordinates:
757 Definition and functional approximations. *Journal of Geophysical Research:*
758 *Space Physics*, *119*(9), 7501–7521. doi: 10.1002/2014JA020264
759 Shibata, T., Matsuya, H., & Hoashi, J. (2000). *Ion composition in the auroral*
760 *lower F-region inferred from residuals of ion temperature profiles observed with*
761 *EISCAT* (Vol. 25; Tech. Rep. No. I). doi: 10.1016/S0273-1177(99)00919-9
762 Takada, M., Seki, K., Ogawa, Y., Keika, K., Kasahara, S., Yokota, S., ... Shino-
763 hara, I. (2021). Low-Altitude Ion Upflow Observed by EISCAT and its
764 Effects on Supply of Molecular Ions in the Ring Current Detected by Arase
765 (ERG). *Journal of Geophysical Research: Space Physics*, *126*(5), 1–12. doi:
766 10.1029/2020JA028951
767 Tesfaw, H. W., Virtanen, I. I., Aikio, A. T., Nel, A., Kosch, M., & Ogawa, Y.
768 (2022). Precipitating Electron Energy Spectra and Auroral Power Estimation
769 by Incoherent Scatter Radar With High Temporal Resolution. *Journal of Geo-*
770 *physical Research: Space Physics*, *127*(4), 1–18. doi: 10.1029/2021ja029880
771 Troshichev, O., Janzhura, A., & Stauning, P. (2006, 5). Unified PCN and PCS
772 indices: Method of calculation, physical sense, and dependence on the IMF
773 azimuthal and northward components. *Journal of Geophysical Research: Space*
774 *Physics*, *111*(5). doi: 10.1029/2005JA011402
775 Virtanen, I. I., Tesfaw, H. W., Roininen, L., Lasanen, S., & Aikio, A. (2021).
776 Bayesian Filtering in Incoherent Scatter Plasma Parameter Fits. *Jour-*
777 *nal of Geophysical Research: Space Physics*, *126*(3), 1–13. doi: 10.1029/
778 2020JA028700
779 Zettergren, M., Semeter, J., Burnett, B., Oliver, W., Heinselman, C., Blelly, P. L.,
780 & Diaz, M. (2010). Dynamic variability in F-region ionospheric composi-
781 tion at auroral arc boundaries. *Annales Geophysicae*, *28*(2), 651–664. doi:
782 10.5194/angeo-28-651-2010